applied sciences

MDPI

Article

Collaborative Design of Static and Vibration Properties of a Novel Re-Entrant Honeycomb Metamaterial

Jiawang Yong [1], Yiyao Dong [1], Zhishuai Wan [2,*], Wanting Li [1] and Yanyan Chen [1]

[1] Department of Traffic Engineering, Beijing University of Technology, Beijing 100124, China; yongjw@bjut.edu.cn (J.Y.); dongyiyao@emails.bjut.edu.cn (Y.D.); liwting@emails.bjut.edu.cn (W.L.); cdyan@bjut.edu.cn (Y.C.)

[2] Beijing Key Laboratory of Lightweight Multi-Functional Composite Materials and Structures, Institute of Advanced Structure Technology, Beijing Institute of Technology, Beijing 100081, China

* Correspondence: wanzhishuai@bit.edu.cn; Tel.: +86-010-6891-1676

Abstract: A novel re-entrant honeycomb metamaterial based on 3D-printing technology is proposed by introducing chiral structures into diamond honeycomb metamaterial (DHM), named chiral-diamond-combined honeycomb metamaterial (CDCHM), and has been further optimized using the assembly idea. Compared with the traditional DHM, the CDCHM has better performance in static and vibration isolation. The static and vibration properties of the DHM and CDCHM are investigated by experiments and simulations. The results show that the CDCHM has a higher load-carrying capacity than that of the DHM. In addition, the vibration isolation optimal design schemes of the DHM and CDCHM are examined by experiments and simulations. It is found that the vibration suppression of the CDCHM is also improved greatly. In particular, the optimization approach with metal pins and particle damping achieves a wider bandgap in the low-frequency region, which can strengthen the suppression of low-frequency vibrations. And the introduction of particle damping can not only design the frequency of the bandgap via the alteration of the dosage, but also enhance the damping of the main structure. This work presents a new design idea for metamaterials, which provides a reference for the collaborative design of the static and vibration properties of composite metamaterials.

Keywords: metamaterial; re-entrant honeycomb; static properties; bandgap; vibration isolation

Citation: Yong, J.; Dong, Y.; Wan, Z.; Li, W.; Chen, Y. Collaborative Design of Static and Vibration Properties of a Novel Re-Entrant Honeycomb Metamaterial. *Appl. Sci.* **2024**, *14*, 1497. https://doi.org/10.3390/app14041497

Academic Editors: Luís Godinho and Javier Redondo

Received: 15 December 2023
Revised: 31 January 2024
Accepted: 9 February 2024
Published: 12 February 2024

1. Introduction

Metamaterials are artificial new materials with a periodic lattice arrangement, and their material properties can be artificially interfered with and adjusted through microstructural design to obtain supernatural properties that cannot be obtained in nature, such as negative stiffness [1–6], negative thermal expansion [7–9] and a zero Poisson or negative Poisson ratio [10–16]. Due to the above excellent properties, metamaterials have been highly used in the domains of mechanics [17–20], acoustics [21–24], electromagnetism [25–27], etc.

The mechanical properties directly affect the service life and application range of the metamaterials, and many scholars have studied the mechanical properties of metamaterials. Wang et al. [28] explored the elastic properties of a metamaterial composed of returnable hexagonal cells in two orthogonal directions. Davood et al. [29] adopted the finite element method (FEM) to study the elastic properties of chiral, antichiral and hierarchical honeycomb metamaterials. Wu et al. [30] proposed an innovative hierarchical antitetrachiral metamaterial which exhibited great tunability in the elastic modulus and Poisson's ratio. He et al. [31] designed a novel returnable honeycomb metamaterial based on the idea of "replacing straight with curved", and used a multi-island genetic algorithm to optimize the parameters of the metamaterial and improve its mechanical properties. With the wide application of metamaterials in various fields, some complex projects have put forward the requirements of multifunctions that cannot be met by common metamaterials.

These requirements led to the research on metamaterials with composite configurations by many scholars. In the work by Novaka et al. [32], a composite metamaterial with an expanded cellular structure and silicon material was presented, and its mechanical properties were investigated under quasistatic and quasidynamic compression conditions. The findings revealed that the presented composite metamaterial exhibited better performance in stiffness and energy absorption than that of the metamaterial made of a single material. Quan et al. [33] designed and prepared a composite metamaterial made of a continuous fiber-reinforced thermoplastic composite (CFRTPC) and pure polylactic acid (PLA), and evaluated its mechanical properties using experimental and simulation methods. It was found that the stiffness of the designed composite metamaterial increased compared with that of the pure PLA metamaterial. Chronopoulos et al. [34] proposed a honeycomb metamaterial, adding negative stiffness elements on the inclusions. The range of the negative stiffness of the metamaterial was widened by adding negative stiffness elements appropriately, and the mechanical properties and vibration-suppression properties were improved. These works indicate that the metamaterials with a composite configuration and multimaterial provide a useful design method to meet the multifunction requirements.

Vibration properties are one of the most important characteristics of metamaterials, and the bandgap characteristics of metamaterials have an evident impact on the vibration-reduction effect, and have been a hot topic in recent years [35–37]. There are two main mechanisms of bandgap formation in metamaterials: Bragg scattering and local resonance [38]. Among them, the local resonance effect can promote the generation of a low-frequency bandgap, which can be explained by the mass–spring physics principle. In this principle, the metamaterial structure is equivalent to a "mass–spring" system, in which the natural frequencies of each order and the upper and lower bounds of the bandgap are determined by the equivalent mass and equivalent stiffness [39]. Mukherjee et al. [40] designed a new honeycomb lattice metamaterial by combining the traditional and additive material lattices, and its bandgap performed better than the traditional honeycomb metamaterial in the low-frequency region. Based on the re-entrant honeycomb metamaterials, Gao et al. [41] proposed a new type of re-entered negative Poisson's ratio metamaterial with rings instead of connection points, and the bandgap properties of the metamaterial were analyzed and optimized according to the mode theory. Liu et al. [42] adopted the FEM to survey the band structure of a two-material triangular re-entrant honeycomb metamaterial with an adjustable thermal expansion coefficient. Ding et al. [43] proposed an isotactic chiral metamaterial with a Thomson scattering-induced bandgap, which generated a broad bandgap in the low-frequency region. Xiang et al. [44] studied the vibration performance of three-dimensional reverse-chiral auxiliary metamaterial under quasistatic conditions through experiments and simulations, and the results showed that the metamaterial had a good performance in vibration suppression. Bergamini et al. [45] introduced the concept of tacticity in spin–spin-coupled chiral phononic crystals. By aligning the centers of adjacent chiral structures in opposite directions, the nature of the coupling between the spins of the atoms in the chain was changed. Thus, it had a good vibration-suppression performance at a low frequency. These works show that low-frequency bandgaps can be achieved by reducing the local stiffness, increasing the local mass of the metamaterials or changing the arrangement of the unit structures. The superior properties of metamaterials with different structures are manifested in different aspects. Therefore, it is an innovative work to integrate two or more single-structural metamaterials to design a new metamaterial with the advantages of all single structures at the same time. In this work, we proposed a novel re-entrant honeycomb metamaterial based on the idea of assembly, which improved the load-bearing capacity of the metamaterial by introducing chiral structures into the conventional diamond structure. Moreover, circular rings were arranged at all the connecting nodes of the proposed metamaterial, and metal pins or particle damping were assembled into the rings to further optimize the overall stiffness of the metamaterial, and excellent bandgap properties in both the high- and low-frequency ranges were obtained. The bandgap properties of the metamaterials are figured by simulation method, and the

influence of the design parameters (including the different sizes of the ring and pin, and the different materials of the pin) on the bandgap properties is also discussed to provide a bandgap adjustment method for meeting the different requirements in engineering applications. Meanwhile, with the different bandgaps of metamaterials generated from the above method, the vibration-suppression performance of the metamaterials was evaluated and compared by simulations and experiments, with a particular concern on the particle damping scheme. In addition, the static properties of the metamaterials, which affect the load-bearing capacity directly, are studied and validated by the combination method of the simulation and experiment.

The rest of the paper is organized as follows. Section 2 describes the geometric structure and design ideas of the novel re-entrant honeycomb metamaterials. Section 3 shows the static properties of the proposed metamaterials and discusses the influence parameters. Section 4 investigates the bandgap properties of the proposed metamaterial and explores its adjustment methods. Section 5 verifies the vibration-isolation performance of the optimized metamaterials through simulation and experiment. Conclusions are given in Section 6.

2. Geometrical Configuration of the CDCHM

In this section, the design method for the CDCHM, together with the geometric structure characteristics of the CDCHM and DHM, are explained. Moreover, the geometric parameters and assembly methods of the metamaterials with different configurations are discussed.

As shown in Figure 1a, the traditional DHM is completely connected by a straight rod, which has a very small stiffness and is easy to deform, so its carrying capacity is very weak. The DHM was improved to the CDCHM, as shown in Figure 1b, by embedding the chiral structure into the traditional configuration, and the chiral structure acted as an internal support to improve the stiffness of the metamaterial. In order to further obtain the low-frequency vibration-suppression ability, metal pins were added to the chiral structure to make a further improvement, as shown in Figure 1c, achieving the collaborative optimization of a high-load-bearing capacity and an excellent vibration-isolation performance.

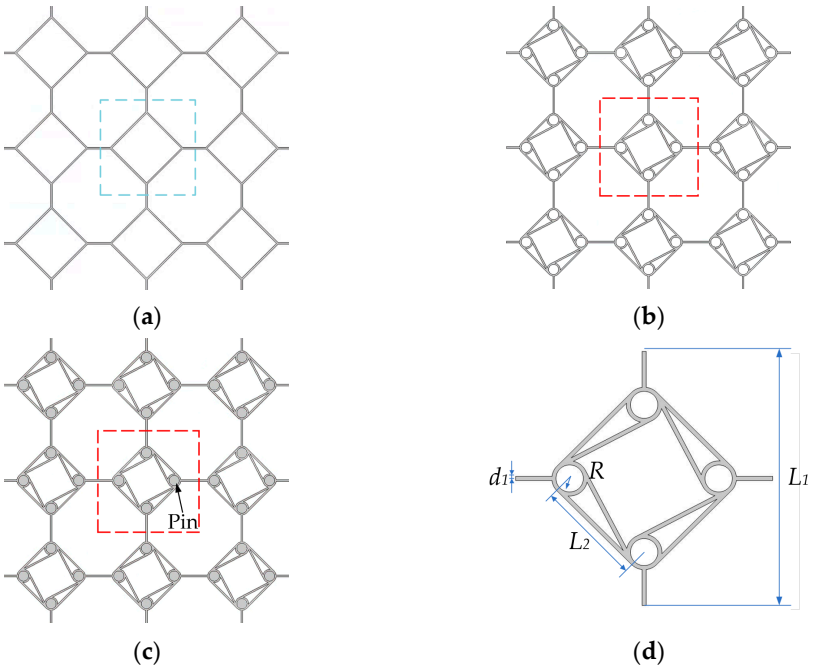

Figure 1. Structure diagrams of the (**a**) DHM; (**b**) CDCHM; (**c**) CDCHM with mental pins; (**d**) schematic diagram of the geometric parameters of the CDCHM.

When the unit cell size is small, there are the problems of high difficulty and large errors in processing and manufacturing. Moreover, when the unit size is large, the overall size of the periodically arranged metamaterial may exceed the height and width of the testing machine, which makes it difficult to conduct experiments. Therefore, considering the limitations of the machining accuracy and test equipment, and combining the number of unit cells arranged in the horizontal and vertical directions, the parameters of the CDCHM are designed using the values listed in Table 1 to ensure the accuracy and convenience of the experiments. The parameters of the CDCHM are shown in Figure 1d, where L_1 is length of the entire unit, L_2 denotes the distance between two adjacent circles of an embedded chiral structure, R represents inner diameter of the ring, d_1 stands for the width of the wall and t is the thickness of the unit cell. The overall dimensions of the unit cell of the DHM and CDCHM are the same.

Table 1. Geometric parameters of a unit cell.

L_1 (mm)	L_2 (mm)	R (mm)	d_1 (mm)	t (mm)
75.158	40	4	1.2	20

3. Static Properties of the Proposed Metamaterials

In this section, the static properties of the metamaterials mentioned above are investigated via simulation and experiment. Firstly, the material parameters and experimental equipment are described. Subsequently, the static compression simulations of the CDCHM and DHM are conducted. Then, the static compression experiments of the CDCHM and DHM are carried out, and the influence of the design parameters on the static properties of the CDCHM is further investigated, which provides a reference for the optimization of the metamaterials.

3.1. Analysis of Static Properties of the Proposed Metamaterials

In order to systematically study the static properties of the CDCHM, static compression tests were performed on the metamaterials using both experimental and simulation methods. The DHM and CDCHM used in the experiment were made by a company named WENEXT (Shenzhen, China) using 3D-printing technology; the original material is plastic. The printed DHM and CDCHM specimens had the same dimensions of 375.79 × 450.95 × 20.00 mm, and the masses of the DHM, CDCHM and CDCHM with copper pins were 0.809 kg, 0.943 kg and 2.02 kg, respectively. Figure 2 represents the simulation and experimental specimens; the blue blocks at the top and bottom ends of the structure are aluminum strips which serve as compression contact surfaces to apply pressure and fix the constraints. The blue circular filling in the ring represents the metal pin. The material properties are listed in Table 2.

The 2D model shown in Figure 2 was constructed using ABAQUS 2018 to simulate the static compression of the metamaterials. The wall thickness of the CDCHM is 1.2 mm. In order to guarantee the simulation precision and to reduce the computational burden, the maximum size of the finite element is 0.3 mm. A fixed constraint was applied to the bottom aluminum strip, and the load force F, shown in Figure 2, was applied to the center of the upper aluminum strip for the simulation.

Table 2. Material properties.

Materials	Density (kg/m^3)	Young's Modulus (MPa)	Poisson's Ratio
Plastic	2650	1.12×10^4	0.42
Aluminum	2700	7.10×10^4	0.33
Copper	8900	1.17×10^5	0.33
Tungsten	19,350	4.11×10^5	0.28

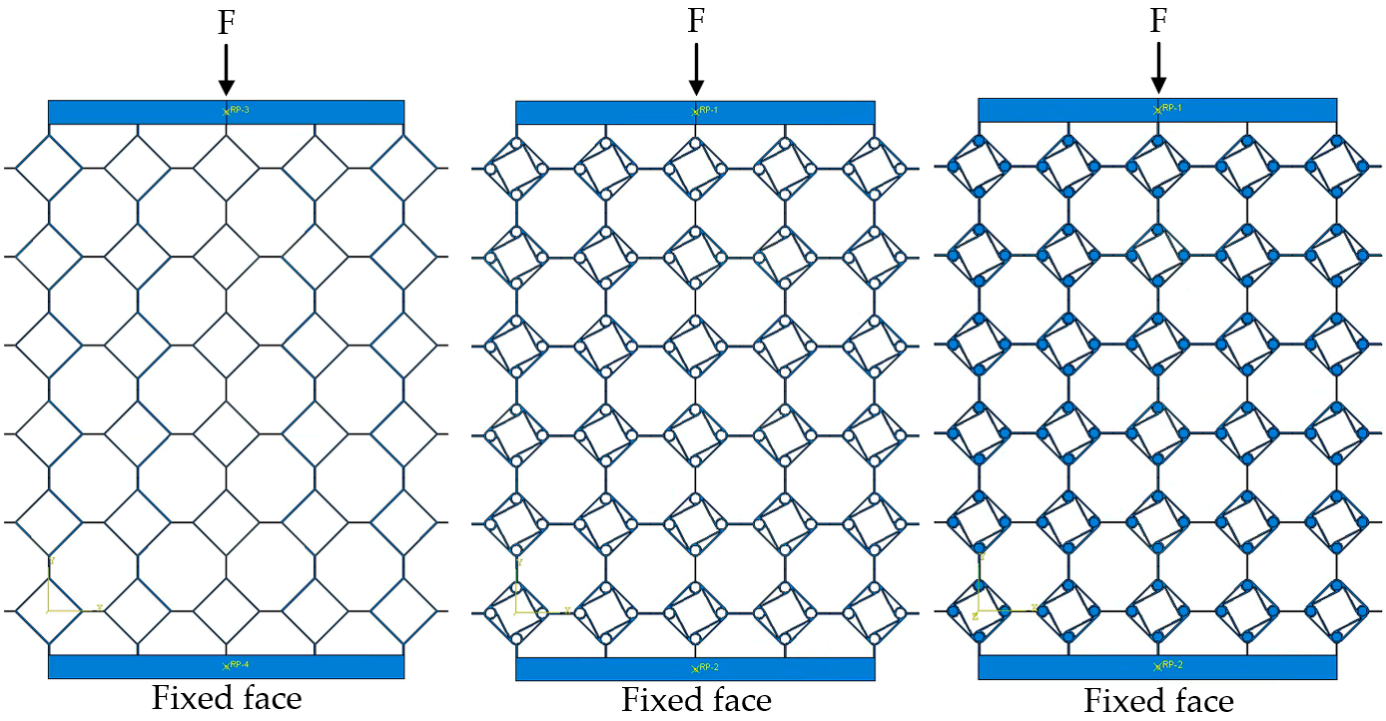

Figure 2. Static compression test diagram.

The static compression tests of the mentioned metamaterials were carried out by the Instron Legend 2367 universal testing machine, shown as Figure 3a, and the experiments were conducted under the same loading conditions with the above simulation settings. The compression displacement gradually increased from 0 until it stopped when the specimen failed.

Figure 3b represents the stress–strain curves obtained from the static compression experiment and simulation of the DHM. The two results have the same trend and high consistency, and the morphology of the simulated and experimental specimens is highly similar under the same deformation degree, shown by pictures A–C in Figure 3b. The results indicate that the simulation method is reliable.

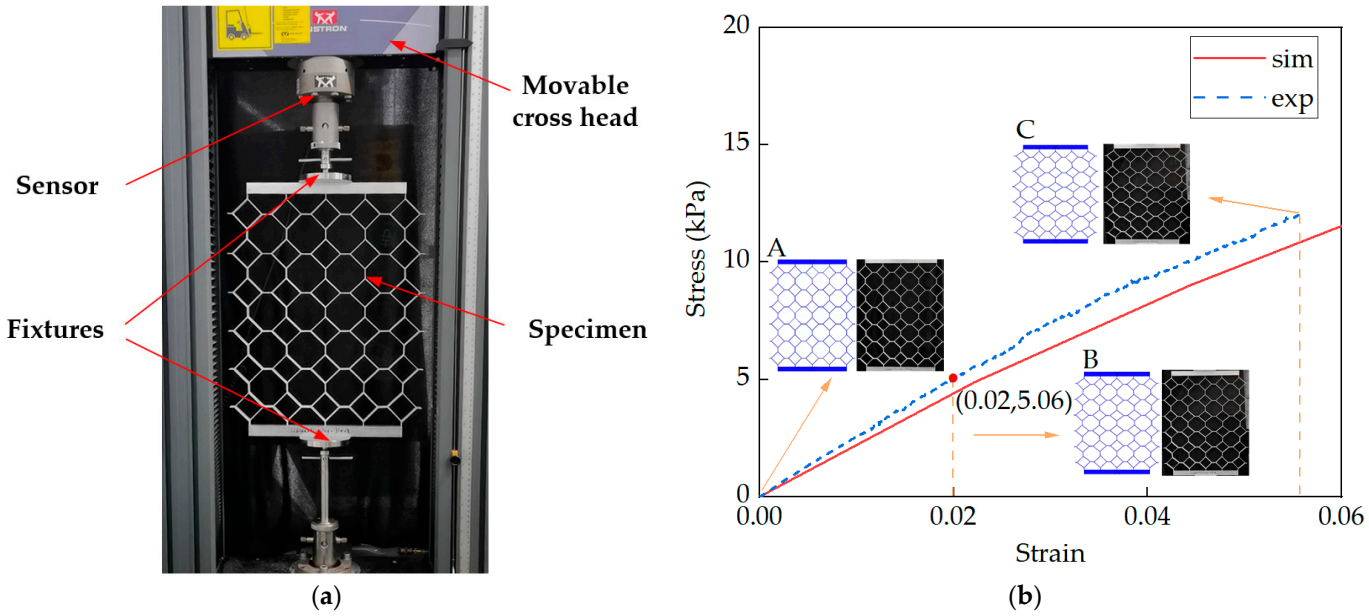

Figure 3. *Cont.*

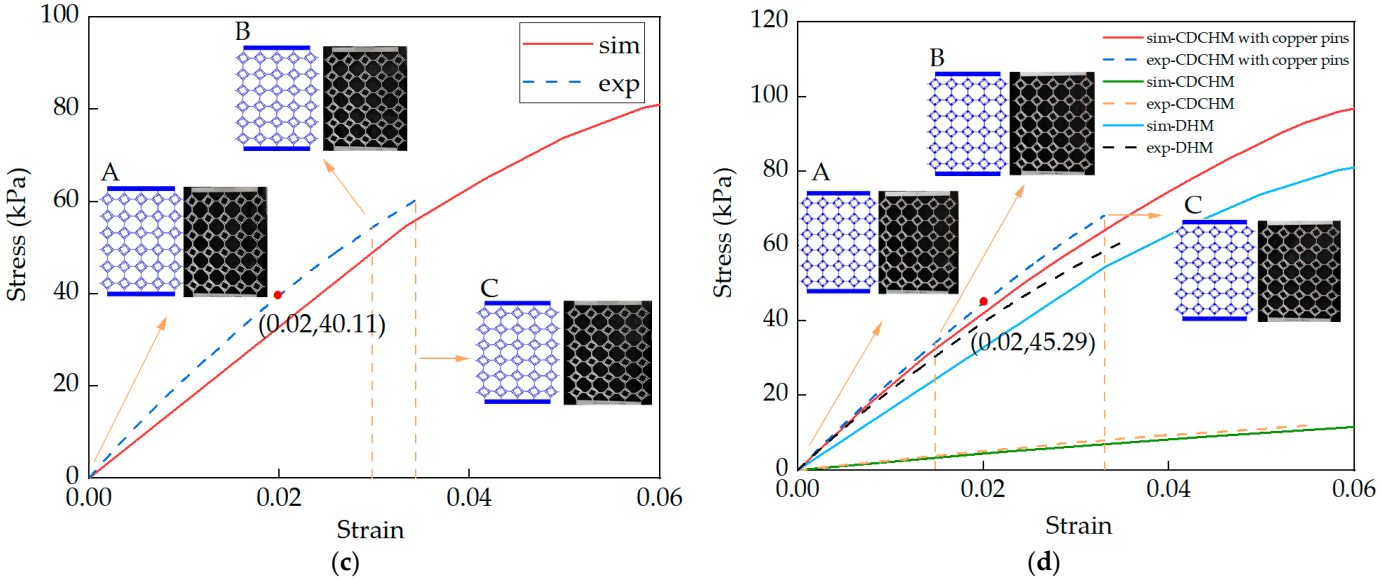

Figure 3. The static compression test of the metamaterials: (**a**) experimental equipment; (**b**) the stress–strain curve of the DHM; (**c**) the stress–strain curve of the CDCHM; (**d**) the stress–strain curves of the CDCHM with the metal pins, the CDCHM and the DHM.

The results of the static compression simulations and experiments of the CDCHM and CDCHM with the metal pins are shown in Figure 3c,d. It can be seen from Figure 3b–d that the stress–strain curves of the metamaterials vary approximately linearly at the initial compression stage. When the structures have been deformed by 2%, the deformation stress corresponding to the DHM is 5.06 KPa, and that corresponding to the CDCHM is 40.11 KPa, which clearly demonstrates that the load-carrying capacity of the CDCHM has been significantly increased by approximately 800%, and the mass is only increased by about 16.6%. However, the load-bearing capacity of the CDCHM with the metal pins is barely enhanced based on the CDCHM, owing to the deformation of the CDCHM mainly being concentrated in the part with the connecting rods.

3.2. Analysis of the Influence of Design Parameters

It has been confirmed in the previous sections that the static properties of the CDCHM are superior to the DHM. In the following section, the effects of the design parameters (including the ring size, the radius of the metal pin and the material of the pin) on the statics of the CDCHM are investigated.

Figure 4a–c show the static compression simulation results of the CDCHM with different ring radii, different metal pin sizes and different metal pin materials, respectively. Due to the characteristics of the specimen structure, the static compression process is roughly divided into two parts. The stress curve of the first half shows a linear trend, while the curve shows a nonlinear trend when the compression reaches a certain degree. The deformations of the samples under different loads can be seen in Figure 4a–c, respectively. With the increase in the radius of the ring, the slope of the stress curve increases gradually, which indicates that the increase in the radius improves the stiffness of the metamaterial. Figure 4c shows that changing the material of the metal pin has little effect on the static properties of the CDCHM. From Figure 4d, it can be seen that, with the introduction of the ring structure, the stiffness of the CDCHM is greatly enhanced compared with the DHM, the metal pins can further enhance the stiffness of the metamaterials and, when the strain is larger than a threshold, the stiffness of the metamaterials is quasizero.

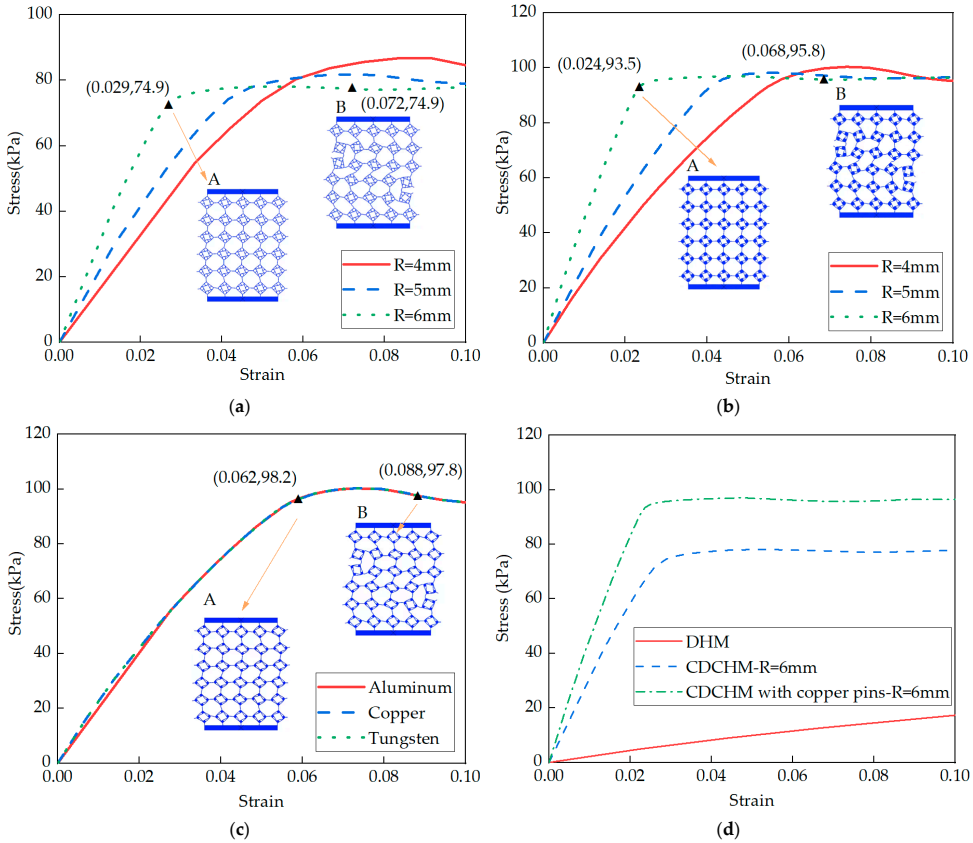

Figure 4. Comparison of static compression results: (**a**) different ring sizes of the CDCHM; (**b**) different radii of the pins of the CDCHM; (**c**) different materials of the CDCHM; (**d**) DHM, CDCHM with a ring radius of 6 mm and the CDCHM with a copper pin radius of 6 mm.

4. Vibration Properties of the Proposed Metamaterials

When the elastic wave propagates in a periodic structure, bandgaps are generated within the frequency range where the wave vectors are attenuated, while wave vectors outside the bandgap are permitted to propagate, leading to vibration filtering characteristics. The bandgap plays an important role for the vibration properties of metamaterials, and the bandgap properties of the proposed metamaterial are examined in this section. Firstly, the propagation mechanism of the elastic waves in the metamaterials is described, and Bloch's theorem is adopted to solve the band structure of the metamaterials. Afterwards, the bandgap characteristics of the DHM and CDCHM are analyzed, and the influence of the design parameters is further discussed.

Based on the equations of the elastic dynamics, the transfer of elastic waves in a 2D structure is expressed as [46]:

$$\nabla[\lambda(\boldsymbol{r}) + 2G(\boldsymbol{r})][\nabla \boldsymbol{u}] - \nabla \times [G(\boldsymbol{r})\nabla \times \boldsymbol{u}] = \rho \ddot{\boldsymbol{u}} \tag{1}$$

in which $\boldsymbol{u}$ represents the displacement vector; $\boldsymbol{r}$ denotes the position vector; ∇ stands for the Hamiltonian differential operator; ρ is the mass density; λ and G stand for Lame' constants.

According to the Bloch theorem, the displacements of all discrete nodes in a unit cell after setting periodic boundary conditions should satisfy the following expressions:

$$\boldsymbol{u}(\boldsymbol{r}, k) = \boldsymbol{u}(\boldsymbol{r}) e^{i(\boldsymbol{k}\boldsymbol{r} - \omega t)} \tag{2}$$

$$\boldsymbol{u}(\boldsymbol{r} + \boldsymbol{R}) = \boldsymbol{u}(\boldsymbol{r}) \tag{3}$$

where $\boldsymbol{k}$ stands for the wave vector; $\boldsymbol{u}$ denotes the displacement vector; $\boldsymbol{R}$ indicates the lattice vector; ω represents the angular frequency.

According to Equations (2) and (3), the eigenvalue equation of the local resonant unit cell after the limit of the periodic boundary conditions is derived as follows:

$$\left(\boldsymbol{K} - \omega^2 \boldsymbol{M}\right)\boldsymbol{U} = 0 \tag{4}$$

in which $\boldsymbol{K}$ stands for the stiffness matrix, $\boldsymbol{M}$ is the mass matrix and $\boldsymbol{U}$ represents the displacement vector of the nodes.

4.1. Bandgap Characteristics

The bandgap properties of the metamaterials are figured by the multiphysics software COMSOL 6.0. The structures of the unit cells are shown in Figure 5a and the irreducible Brillouin region boundary (O→M→Γ→O) is defined in Figure 5b. A series of characteristic frequencies are determined corresponding to the propagation of the wave vector $\boldsymbol{k}$, and the band structures of the metamaterials are achieved for further analysis.

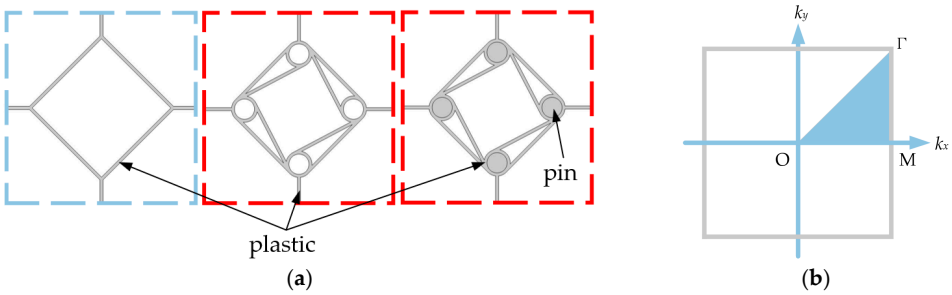

Figure 5. Structure diagram for bandgap analysis: (**a**) unit cells of the DHM, CDCHM and CDCHM with metal pins; (**b**) irreducible Brillouin zone of the periodic lattice.

Figure 6 shows the elastic wave dispersion curves of the DHM, CDCHM and CDCHM with the metal pins. There is a one-to-one correspondence between the scanning parameters 0→1→2→3 and O→M→Γ→O in the irreducible Brillouin region in Figure 6. The dispersion curves suggest that the DHM only has two narrow bandgaps within the range under 10,000 Hz, and its lowest bandgap is nearby at 4100 Hz, which indicates that the DHM has poor vibration-suppression performance at low frequencies. A1–A4 in Figure 7 illustrate the vibration modes corresponding to the marked frequencies in Figure 6b; we have noticed that the mode deformation is the global deformation of the cell, and changing the global mode deformation to the local mode deformation is an effective method to generate a local resonance bandgap.

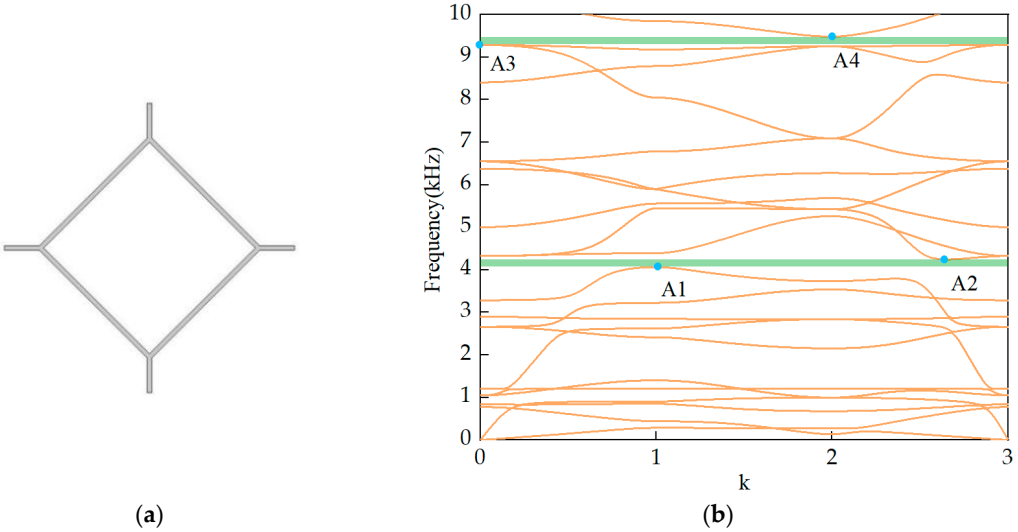

Figure 6. *Cont.*

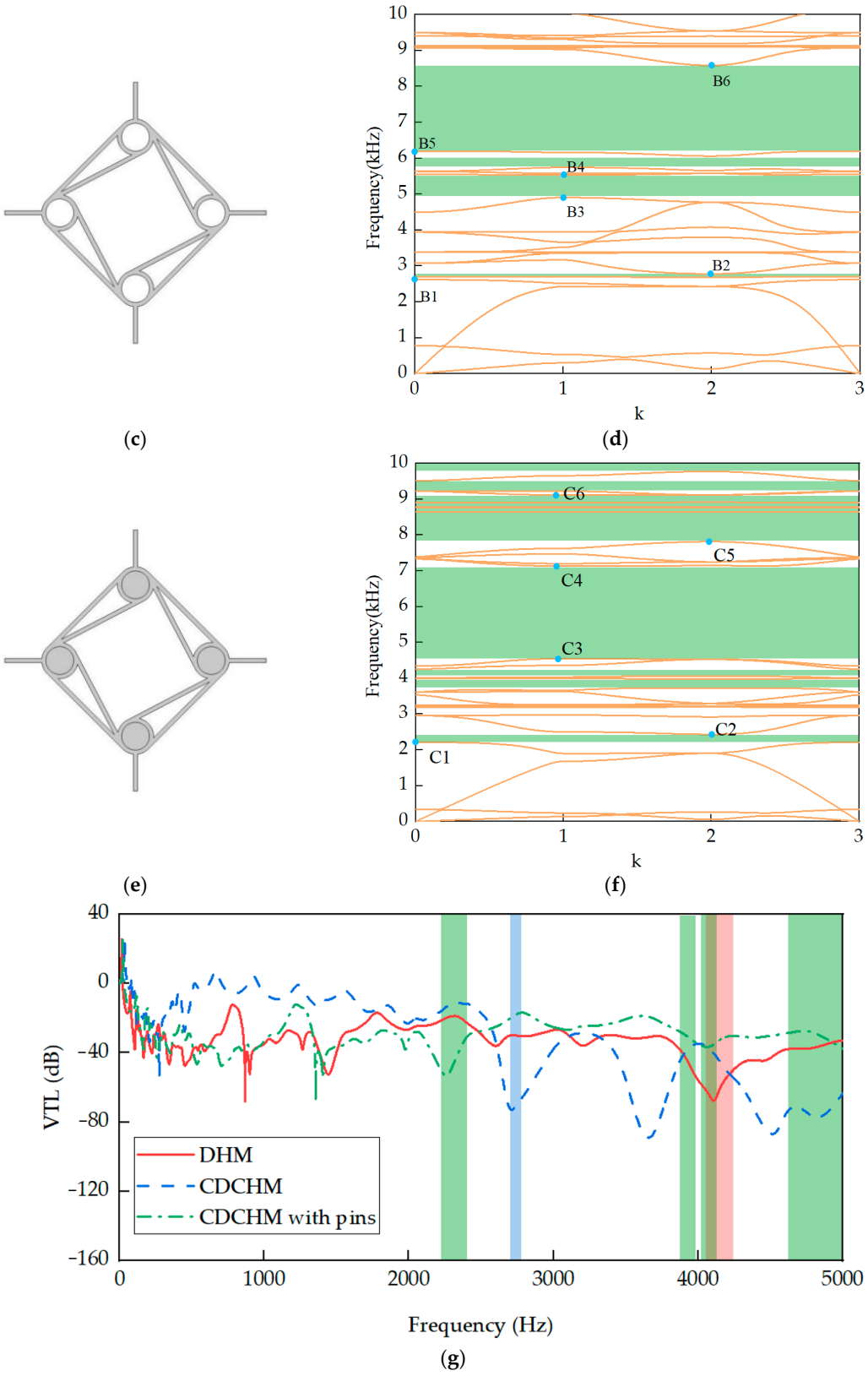

Figure 6. The simulation results of the metamaterials: (**a**,**b**) the dispersion curve of the DHM; (**c**,**d**) the dispersion curve of the CDCHM; (**e**,**f**) the dispersion curve of the CDCHM with the copper pins; (**g**) the VTL curves and bandgaps of the metamaterials.

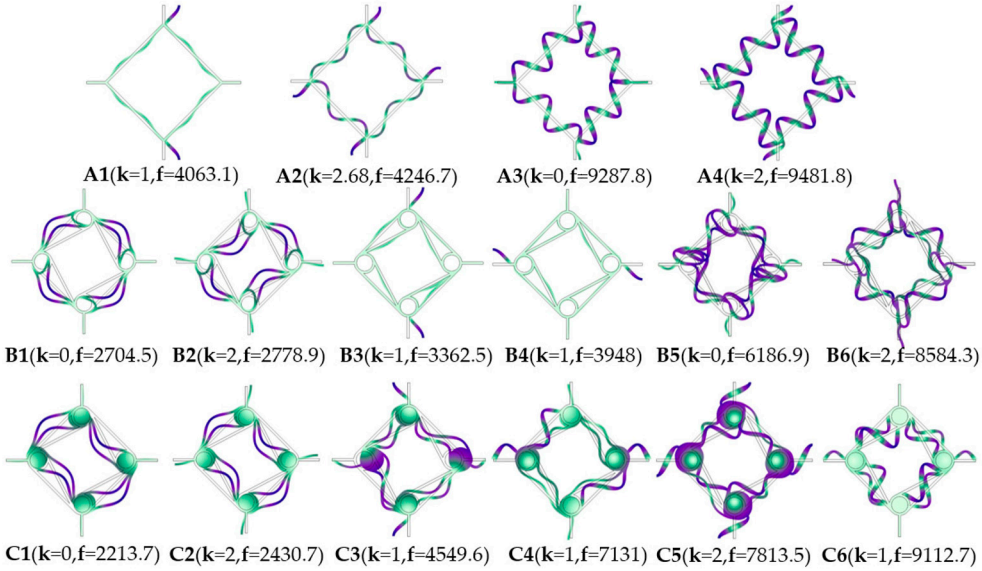

Figure 7. The vibration modes corresponding to the points in Figure 6.

As explained in Figure 6c,d, with a chiral structure assembled into the diamond honeycomb structure, the bandgap properties of the CDCHM are greatly improved compared with the original DHM. The first bandgap of the CDCHM is nearby at 2700 Hz, which means that the modified metamaterial shows a better vibration-suppression effect at low frequencies. Moreover, the inferior limited frequency of the second bandgap of the CDCHM declines from about 9200 Hz to 5000 Hz, along with a wider bandwidth, and the third and fourth bandgaps are generated, and especially the width of the fourth bandgap is very wide, which is from 6187 Hz to 8584 Hz. According to A1–A4 and B1–B4, it is found that the node stiffness of the metamaterial is improved with the introduction of a chiral structure, and the local mode deformations of the cell are generated, which provide better bandgap properties. The metal pins further enhanced the local resonance and generated bandgaps in the lower-frequency range, as shown in Figure 6e,f. The corresponding modes are shown in Figure 7C1–C6.

In order to further analyze the vibration-isolation performance of the metamaterials, the concept of vibration transmission loss (VTL) is introduced to evaluate the vibration-suppression ability, which can be expressed as:

$$\mathrm{VTL} = 20 \times \lg\left(\frac{a_0}{a_i}\right) \tag{5}$$

where a_0 and a_i represent the acceleration amplitudes of the output and input of the metamaterials, respectively.

The VTL simulation results of the metamaterials mentioned above are shown in Figure 6g. We found that the attenuation part of the VTL is in a good correspondence with the bandgap obtained by the COMSOL simulation (highlighted by corresponding colors in the background), so the effectiveness of the two simulation methods can be mutually verified. According to the above analysis, it can be inferred that the ring structure is a key factor affecting the generation of bandgaps, and changing the ring size of the CDCHM may obtain different bandgap characteristics.

4.2. Analysis of the Influence of Design Parameters

It can be concluded from the research in the previous section that the improved way of introducing the chiral structure and adding metal pins effectively optimizes the bandgap characteristics of the DHM. The effects of the structural design parameters on the vibration characteristics of the metamaterials are discussed in this section.

4.2.1. The Influence of Ring Size of Chiral Structure

Figure 8 draws the bandgap properties of the CDCHM with different sizes of rings. As the ring radius of the chiral structure increases from 4 mm to 6 mm, with a resolution of 1 mm, the lower limiting frequency of the bandgap of the metamaterial at a low frequency gradually decreases, the upper limiting frequency of the bandgap gradually increases, resulting in the width increase in the bandgaps. Figure 8e plots the influence of the rings of different sizes on the vibration modes of the first bandgap. It can be observed that the first bandgap of the CDCHM is mainly caused by the deformation of the rod. With the increase in the ring radius, the coupling between the ring and rod is deepened, and the lower bandgap gradually moves to the low frequency. This means that the larger the ring radius, the stronger the vibration-suppression ability of the metamaterial at low frequencies (2000–3000 Hz). Since the size of the chiral ring is limited by the external diamond structure, the maximum radius of the ring is 8 mm, and the lower limit of the first gap of the CDCHM is reduced to 1700 Hz in this ring size, which further proves the universality of the above conclusion.

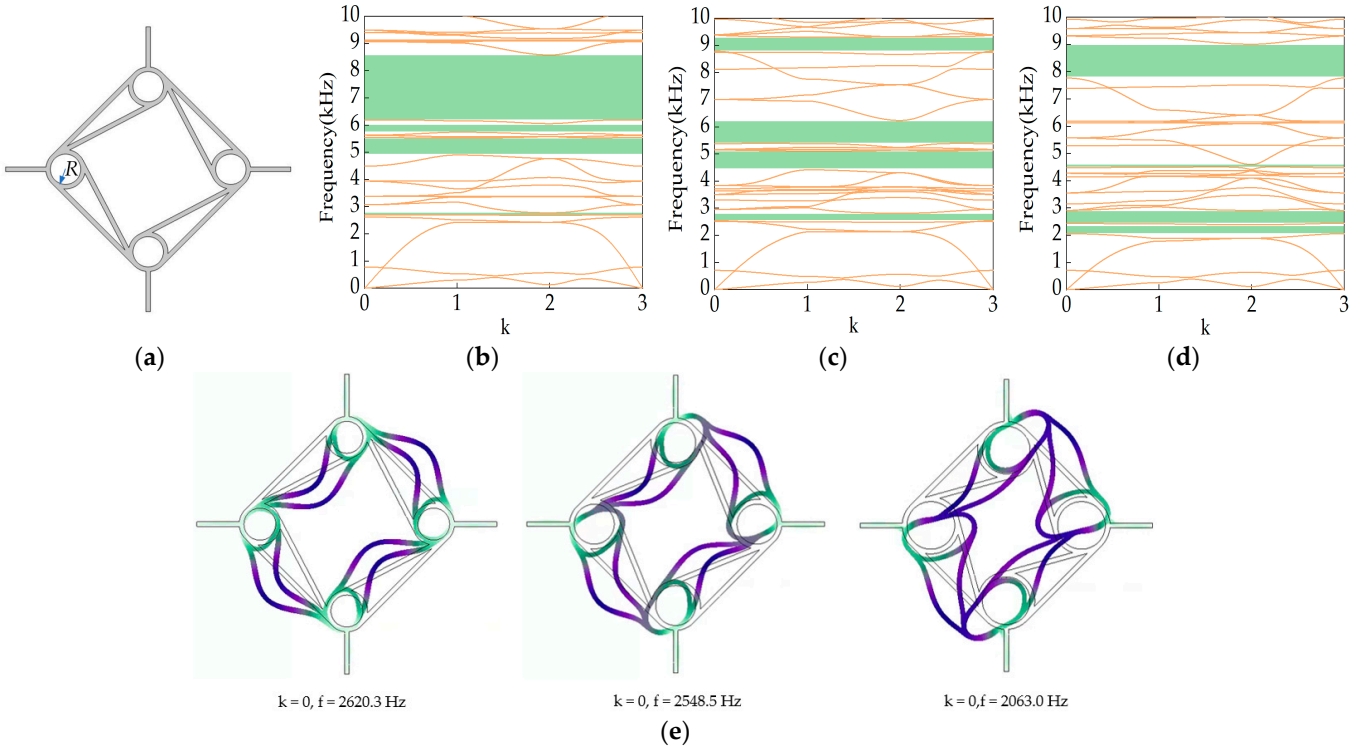

Figure 8. The influence of the ring radius on the bandgaps: (**a**) structure diagram of the CDCHM; (**b**) R = 4 mm; (**c**) R = 5 mm; (**d**) R = 6 mm; (**e**) vibration mode of the first gap.

4.2.2. The Influence of Metal Pin Size

As indicated from Figure 6e,f, the change in the structure mass distribution will affect the bandgap characteristics. Figure 9 depicts the bandgap distributions of the CDCHM inserted with metal pins of different sizes, and the material of the pins is copper. The introduction of copper pins produces local resonance effect between the ring and the copper pins. With the increase in the radius of the copper pins, the local mass of the CDCHM increases, and the local resonance effect is gradually enhanced, resulting in the improvement of the bandgap properties of the CDCHM in the range under 10,000 Hz. Among them, the lower limiting frequency of the first bandgap is reduced to about 1800 Hz, and the width of the first bandgap increases obviously. The proportion of all bandgaps at 1–10,000 Hz increased from about 45.4% to 64.2%. Moreover, when the radius is increased to 8 mm, the proportion of all bandgaps reaches about 71%, and the lower limit of the first

bandgap frequency is 1247 Hz, which indicates that increasing the size of the added metal pin is of great benefit to improve the vibration-suppression ability of the metamaterial without changing the overall structure size.

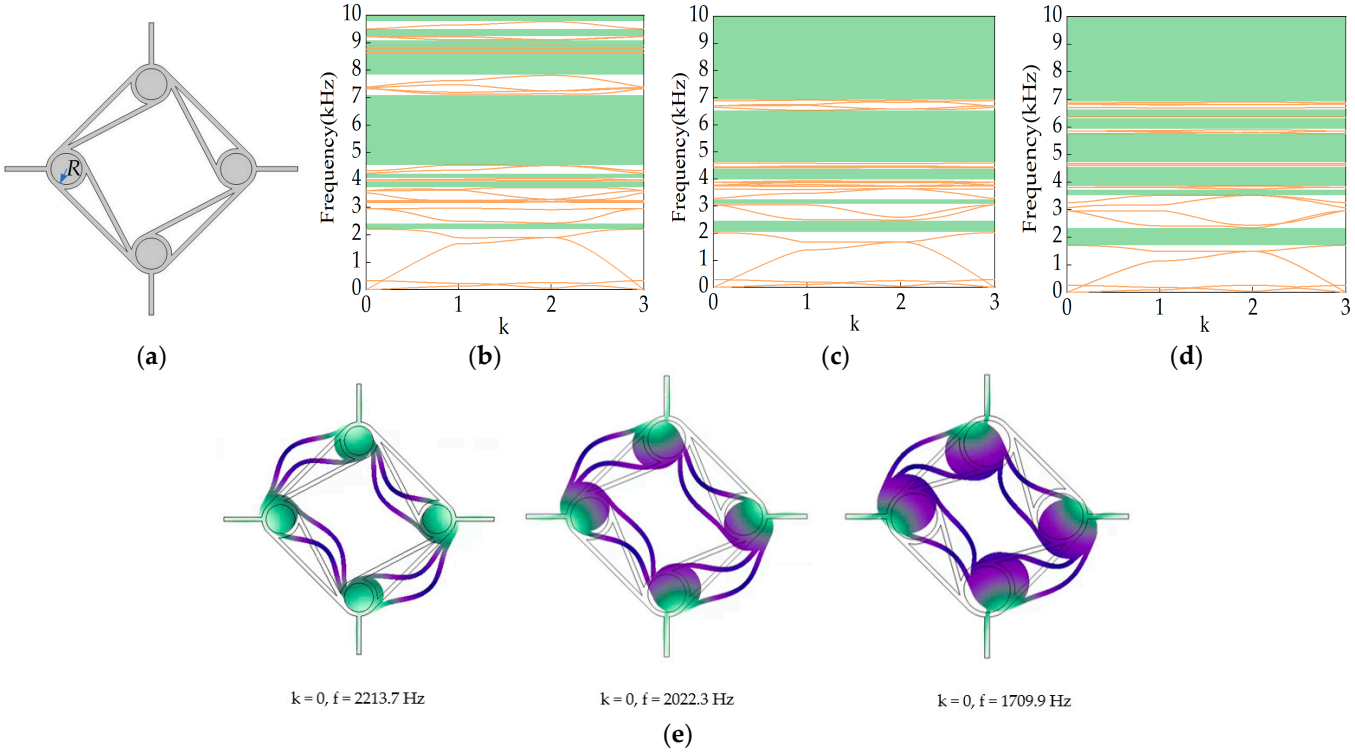

Figure 9. The influence of pin size on the bandgaps. (**a**) Structure diagram of CDCHM, (**b**) R = 4 mm, (**c**) R = 5 mm, (**d**) R = 6 mm; (**e**) vibration mode of the first gap.

4.2.3. The Influence of Pin Material

Through the structure modal analysis, it can be seen that changing the density of the CDCHM metal pins can realize the adjustment of the bandgaps. Figure 10 shows the bandgap characteristics of the CDCHM with metal pins of the same size and different materials (aluminum, copper and tungsten). It can be seen from the vibration modes that determine the first bandgap of the CDCHM with metal pins of different materials depicted in Figure 10e that the introduction of the metal pins produces a local resonance effect between the ring and the metal pins. As the metal pin is successively made of aluminum, copper and tungsten, the density gradually increases, and the CDCHM opens a new bandgap in the low-frequency region below 2000 Hz, which will bring better low-frequency vibration-suppression ability to the CDCHM. On the other hand, the distributed bandgaps in the case of adding low-density metal pins gradually concentrates to form a new bandgap with a wider width after the density increases, especially when the metal pin is made of tungsten due to a significant increase in the density, and the frequency band from 6000 Hz to 10,000 Hz can be almost fully covered by the bandgaps. As the density of the pins increases, the first bandgap gradually moves to the low frequency, and the bandgap width increases from 174 Hz to 219 Hz.

According to the above analysis, the bandgap properties of the metamaterial can be regulated by adopting metal pins made of different materials. It offers a reference for the optimal design of metamaterials so as to meet the requirements of the different vibration absorption frequencies in applications.

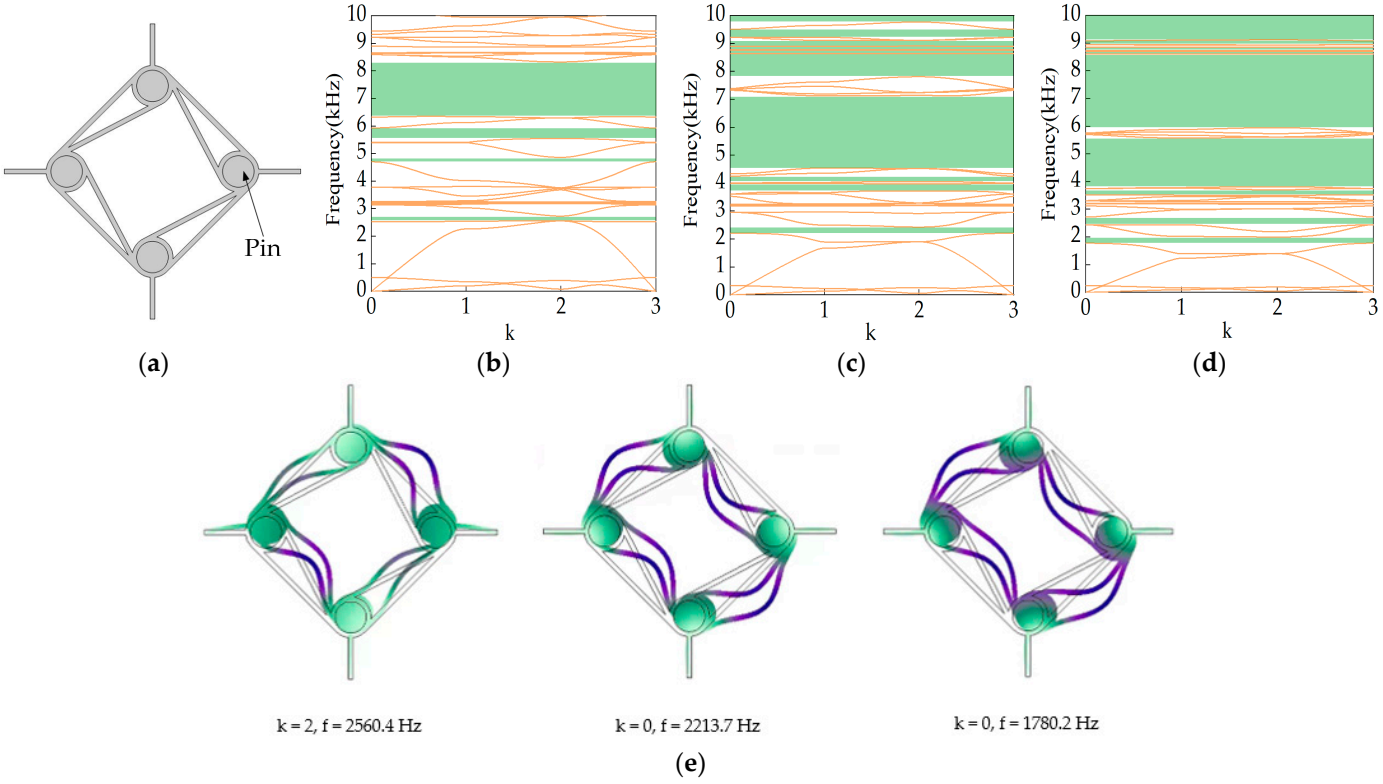

Figure 10. The influence of materials of pins on bandgap: (**a**) structure diagram of the CDCHM; (**b**) aluminum; (**c**) copper; (**d**) tungsten; (**e**) vibration mode of the first gap.

5. Experimental Validation and Further Optimization of Vibration Properties Method

For the main structure of the proposed metamaterials, the bandgap properties can be adjusted by adopting different materials for the pins. However, the density of the metal pins is not continuous, which results in an altered discontinuity of the bandgap frequency. Furthermore, the vibration suppression in the low-frequency band has always been a concern in engineering applications; to be precise, scholars have been widely interested in the ability of metamaterials to suppress low-frequency vibrations, especially to below 2000 Hz. Unfortunately, the bandgap effect of the CDCHM is still not ideal at low frequencies after the introduction of chiral structures, and new optimization methods need to be explored in addition to adding metal pins.

According to the modal theory and the above research on the vibration properties of the metamaterials, adding dense materials to the structure of the CDCHM can simultaneously improve the bearing capacity and vibration-suppression performance. Moreover, according to the modes of the metamaterial, it can be found that the vibration deformation of the chiral structure in the low-frequency region is mainly the local resonance based on the metal pins. Therefore, an optimization method of using particle damping to suppress the vibration of the metamaterial is proposed, and the metal tube with particle damping is introduced into the rings of the CDCHM.

In order to further explore the vibration-suppression ability of the CDCHM and the optimization approach, and verifying the effectiveness and accuracy of the COMSOL and ABAQUS simulation methods, the vibration transmission loss of the proposed metamaterials was tested on the experimental system. Figure 11 shows the experimental system. The input and output signals of the two equipped acceleration sensors were collected at a frequency of 10 kHz, and the signals were converted and transmitted to the computer by the signal converter. The shaker realized the white noise excitation signal generated from the signal generator, and the sweep frequency range was from 2 Hz to 2500 Hz. To more clearly show the trend of the test results, a Kalman filter was designed to process the experimental data.

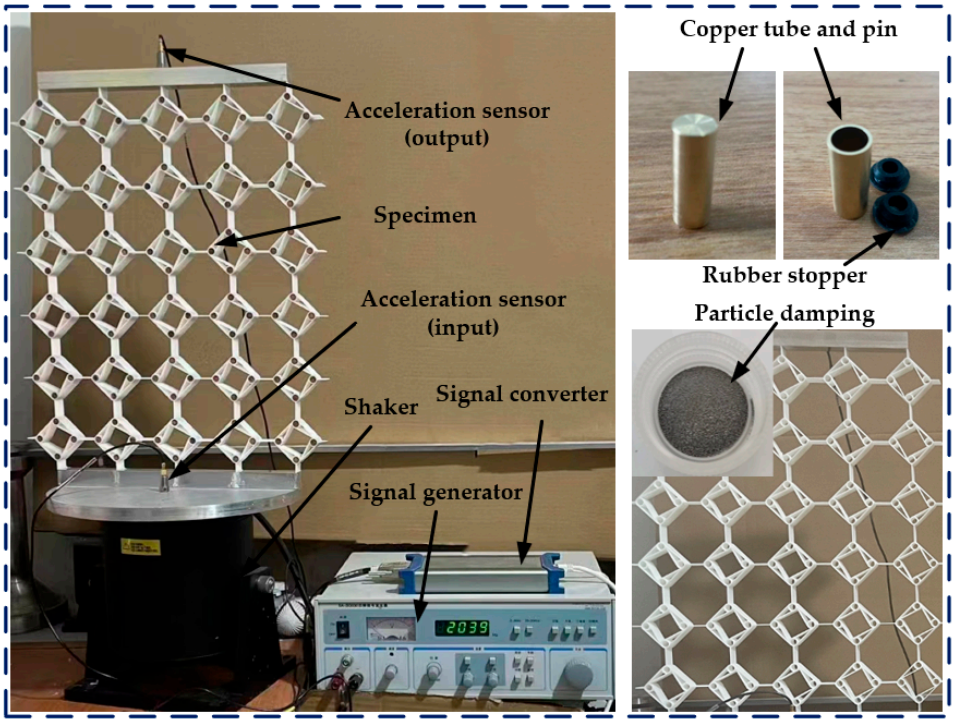

Figure 11. The experimental system of vibration transmission loss.

In this section, a metal tube with particle damping is introduced into the CDCHM to achieve better vibration suppression. Firstly, the vibration characteristics of the proposed metamaterials are tested to verify the simulations. Subsequently, the vibration characteristics of the CDCHM with particle damping are investigated by the experiments.

Figure 12 represents the bandgaps (green color bars) from the simulation and the VTL based on the experiment. As indicated from Figure 12a, the first bandgap suppresses the increasing vibration. Due to the introduction of the chiral structure, the CDCHM has a narrow first bandgap at around 2700 Hz, which is similar to the effect of a dynamic vibration absorber, and the two bandgaps of the CDCHM within 5000 Hz are located near the trough of the VTL curve, as shown in Figure 12b. Figure 12c shows the experiment and simulation results of the CDCHM with the copper pins. It can be seen that the first bandgap is at the attenuation part of the VTL curve. Since the second and third bandgaps are narrow and there is a gap between them, the variation in the VTL curve is not large. Furthermore, the value of the VTL here is close to −20 dB, so it can be considered that the test and simulation correspond to each other. The fourth bandgap in Figure 12c is in the second half of the VTL curve depression, which is caused by the characteristics of the structure itself. Considering that there is a certain gap between the experimental conditions and the ideal conditions of the simulation, and combined with the above analysis, the bandgap obtained by the COMSOL and the VTL curve obtained by the experiment are consistent, so the simulation method can be considered reliable.

The vibration characteristics of the CDCHM with particle damping are tested. In order to prevent particle leakage affecting the accuracy of the results, rubber stoppers are installed at both ends of the ring. Figure 12d shows the experimental VTL results of the CDCHM with particle damping of equal mass to the metal pins. The frequencies of the resonant peaks of the two curves in the low-frequency band from 0 to 1000 Hz are almost equal, and the vibration in the range from 800 Hz to 4500 Hz is suppressed due to the particle damping, especially for the vibration from 800 Hz to 2200 Hz. In addition, the mass of the pipes with particle damping can be adjusted by the dosage of particle damping, and the frequency of the bandgap can change continuously, instead of reinstalling pins of different materials.

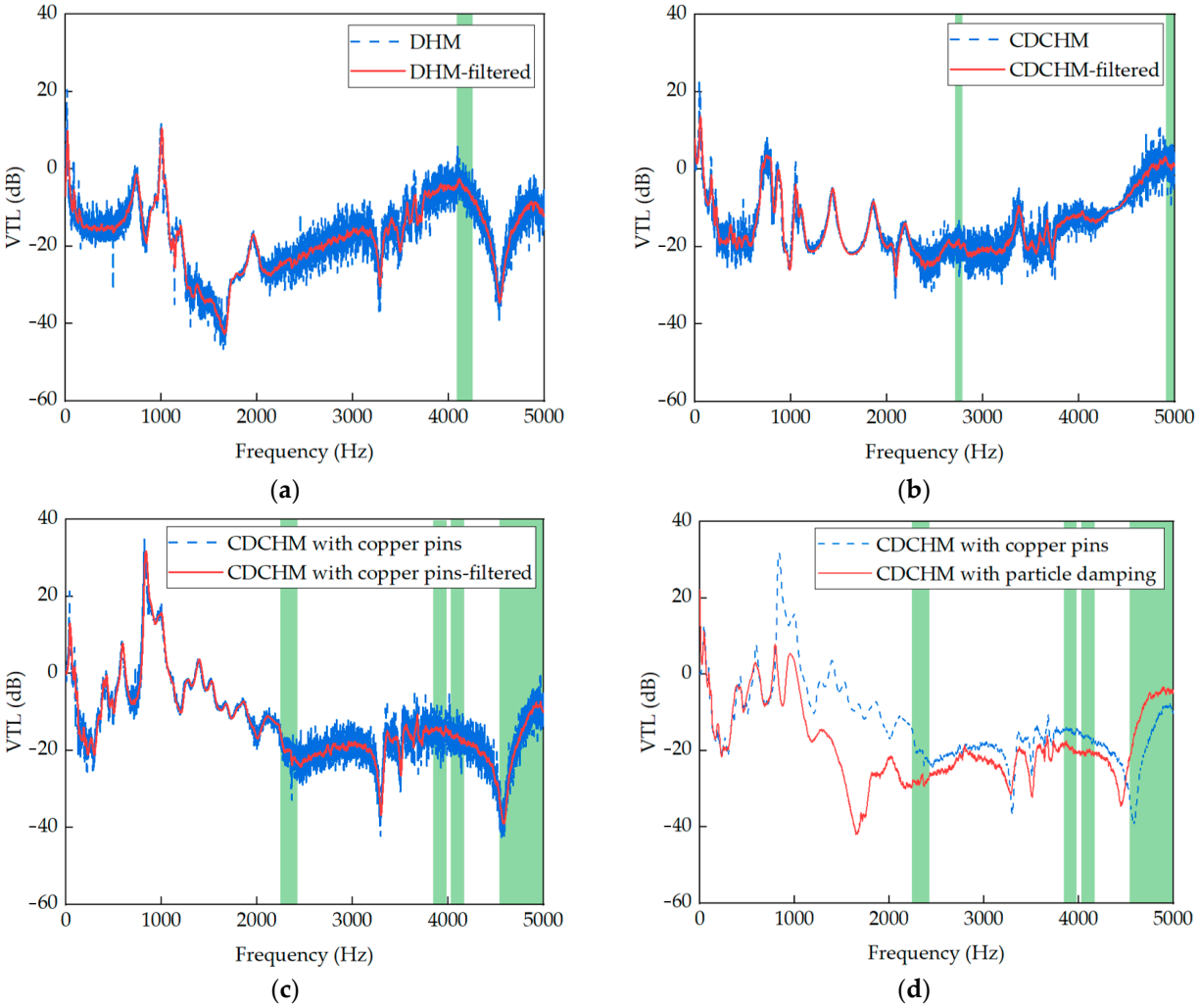

Figure 12. Experimental VTL results of different metamaterials: (**a**) DHM; (**b**) CDCHM; (**c**) CDCHM with the copper pins; (**d**) comparison of the filtering results of the CDCHM with the metal pins and the CDCHM with particle damping.

The VTL value in the figure attenuates obviously near 950 Hz. Compared with the experimental results of the basic CDCHM, the addition of particle damping can effectively improve the ability of the CDCHM to suppress low-frequency vibrations. At the same time, compared with the CDCHM with the metal pins, that with particle damping effectively inhibits the peak values of the VTL within 2500 Hz, which means that the interaction between damping has a better effect on the isolation of low-frequency vibrations.

6. Conclusions and Applications

6.1. Conclusions

This work presents a new re-entrant honeycomb metamaterial, and the proposed metamaterial is purposefully optimized by means of assembling metal pins and particle damping. The static and vibration-isolation properties of the metamaterial are investigated by simulations and experiments. Conclusions are as follows:

1. Compared with the DHM, the load-carrying performance of the CDCHM is improved by approximately 800%, and the mass is only increased by about 16.6%;
2. Increasing the size of the ring structure in the CDCHM can effectively enhance its static performance and vibration-isolation performance at the same time;
3. Adding metal pins to the CDCHM can realize the adjustment of the bandgaps, the larger the size or density of the metal pin and the lower the inferior limited frequency

of the first bandgap; the inferior limited frequency of the first bandgap achieved in this paper is 1709 Hz, and will probably be even lower if the pins are made of a higher-density material;

4. The introduction of particle damping into the CDCHM can further improve the vibration-suppression ability of the metamaterial, and the frequency of the bandgap can be adjusted by the dosage of the particle damping.

The bandgaps of the proposed CDCHM could be designed by changing the assembly material, which provides a reference for the future metamaterial optimization design. In addition, since the focus of this work is the improvement of the carrying capacity and vibration-isolation performance, and the main application targets of the metamaterials proposed in this work are vehicles, ships and other fields that are not sensitive to mass, so equal mass is not taken as a constraint and a lightweight design is not taken into consideration. In future studies, we will improve the research on this point and further improve the design ideas and methods of metamaterial improvement.

6.2. Applications

Compared with high-frequency vibrations, low-frequency vibrations are more common in engineering applications. In this work, the load-bearing capacity and vibration-isolation performance of the traditional configuration were optimized. The load-bearing capacity of the designed metamaterials were greatly improved and the lower limit of the first bandgap of metamaterials were reduced to less than 2000 Hz. These excellent properties enable them to be well applied in the fields of vehicle shock and noise reduction, and aircraft and ship manufacturing.

Author Contributions: Conceptualization, J.Y. and Z.W.; methodology, J.Y and Z.W.; software, Y.D. and W.L.; validation, Y.D., Y.C. and W.L.; formal analysis, J.Y.; investigation, Y.D.; resources, Z.W.; data curation, Y.D.; writing—original draft preparation, J.Y. and Y.D.; writing—review and editing, J.Y. and Z.W.; visualization, W.L.; supervision, Y.C.; project administration, Y.C.; funding acquisition, J.Y. All authors have read and agreed to the published version of the manuscript.

Funding: This research was funded by Beijing Natural Science Foundation (No. 3222003), National Natural Science Foundation of China (No. 52002009), and the State Key Laboratory of Automotive Safety and Energy under Project (No. KF2010).

Institutional Review Board Statement: Not applicable.

Informed Consent Statement: Not applicable.

Data Availability Statement: The data that support the findings of this study are available from the corresponding author upon reasonable request.

Conflicts of Interest: The authors declare no conflicts of interest.

References

1. Tan, X.; Chen, S.; Wang, B.; Tang, J.; Wang, L.; Zhu, S.; Yao, K.; Xu, P. Real-time tunable negative stiffness mechanical meta-material. *Extrem. Mech. Lett.* **2020**, *41*, 100990. [CrossRef]
2. Tan, X.; Chen, S.; Zhu, S.; Wang, B.; Xu, P.; Yao, K.; Sun, Y. Reusable meta-material via inelastic instability for energy absorption. *Int. J. Mech. Sci.* **2019**, *155*, 509–517. [CrossRef]
3. Morris, C.; Bekker, L.; Spadaccini, C.; Haberman, M.; Seepersad, C. Tunable mechanical meta-material with constrained negative stiffness for improved Quasi-Static and Dynamic Energy Dissipation. *Adv. Energy Mater.* **2019**, *21*, 1900163.
4. Tan, X.; Wang, B.; Yao, Y.; Yao, K.; Kang, Y.; Zhu, S.; Chen, S.; Xu, P. Programmable Buckling-based negative stiffness meta-material. *Mater. Lett.* **2019**, *262*, 127072. [CrossRef]
5. Chen, X.; Zhao, J.L.; Deng, J.; Jing, Y.; Pu, H.Y.; Luo, J. Low-frequency enhancement of acoustic black holes via negative stiffness supporting. *Inter. J. Mech. Sci.* **2023**, *241*, 107921. [CrossRef]
6. Tan, X.J.; Wang, B.; Chen, S.; Zhu, S.W.; Sun, Y.G. A novel cylindrical negative stiffness structure for shock isolation. *Compos. Struct.* **2019**, *214*, 379–405. [CrossRef]
7. Yu, H.B.; Wu, W.W.; Zhang, J.X.; Chen, J.K.; Liao, H.T.; Fang, D.L. Drastic tailorable thermal expansion chiral planar and cylindrical shell structures explored with finite element simulation. *Compos. Struct.* **2019**, *210*, 327–338. [CrossRef]

8. Liu, H.T.; Xu, N.; Wang, Y.B.; Wang, L. Three-dimensional enhanced star-shaped honeycombs with negative thermal expansion. *Compos. Struct.* **2022**, *279*, 114772. [CrossRef]
9. Li, X.; Gao, L.B.; Zhou, W.Z.; Wang, Y.J.; Lu, Y. Novel 2D meta-material with negative Poisson's ratio and negative thermal expansion. *Extrem. Mech. Lett.* **2019**, *30*, 100498. [CrossRef]
10. Zhang, X.G.; Ren, X.; Jiang, W.; Zhang, X.Y.; Luo, C.; Zhang, Y.; Xie, Y.M. A novel auxetic chiral lattice composite: Experimental and numerical study. *Compos. Struct.* **2022**, *282*, 115043. [CrossRef]
11. Li, D.; Yin, J.; Dong, L.; Lakes, R.S. Strong re-entrant cellular structures with negative Poisson's ratio. *J. Mater. Sci.* **2018**, *53*, 3493–3499. [CrossRef]
12. Luo, H.C.; Ren, X.; Zhang, Y.; Zhang, X.Y.; Zhang, X.G.; Luo, C.; Cheng, X.; Xie, Y.M. Mechanical properties of foam-filled hexagonal and re-entrant honeycombs under uniaxial compression. *Compos. Struct.* **2022**, *280*, 114922. [CrossRef]
13. Tan, H.L.; He, Z.C.; Li, K.X.; Li, E.; Cheng, A.G.; Xu, B. In-plane crashworthiness of re-entrant hierarchical honeycombs with negative Poisson's ratio. *Compos. Struct.* **2019**, *229*, 111415. [CrossRef]
14. Gao, Q.; Ding, Z.; Liao, W. Effective elastic properties of irregular auxetic structures. *Compos. Struct.* **2022**, *287*, 115269. [CrossRef]
15. Zhang, X.C.; An, C.C.; Shen, Z.F.; Wu, H.X.; Yang, W.G.; Bai, J.P. Dynamic crushing responses of bio-inspired re-entrant auxetic honeycombs under in-plane impact loading. *Mater. Today Commun.* **2020**, *23*, 100918. [CrossRef]
16. He, X.; Yu, J.; Xie, Y. Bi-Material Re-Entrant Triangle Cellular Structures Incorporating Tailorable Thermal Expansion and Tunable Poisson's Ratio. *J. Mech. Robot. Trans. ASME* **2019**, *6*, 11.
17. Zhu, Y.L.; Jiang, S.H.; Zhang, Q.; Li, J.; Yu, C.; Zhang, C.Z. A novel monoclinic auxetic meta-material with tunable mechanical properties. *Int. J. Mech. Sci.* **2022**, *236*, 107750. [CrossRef]
18. Yi, J.L.; Meng, Z.Q.; Chen, J.L.; Chen, C.Q. Dispersive higher harmonic generation and enhancement in mechanical meta-material. *Int. J. Mech. Sci.* **2023**, *246*, 108146. [CrossRef]
19. Mizzi, L.; Attard, D.; Gatt, R.; Farrugia, P.S.; Grima, J.N. An analytical and finite element study on the mechanical properties of irregular hexachiral honeycombs. *Smart Mater. Struct.* **2018**, *27*, 105016. [CrossRef]
20. Zhong, R.C.; Fu, M.H.; Chen, X.; Zheng, B.B.; Hu, L.L. A novel three-dimensional mechanical meta-material with compression-torsion properties. *Compos. Struct.* **2019**, *226*, 111232. [CrossRef]
21. Spadoni, A.; Ruzzene, M.; Gonella, S.; Scarpa, F. Phononic properties of hexagonal chiral lattices. *Wave Motion* **2019**, *46*, 435–450. [CrossRef]
22. Nimmagadda, C.; Matlack, K.H. Thermally tunable band gaps in architected meta-material structures. *J. Sound. Vib.* **2019**, *439*, 29–42. [CrossRef]
23. Bukhari, M.; Barry, O. Simultaneous energy harvesting and vibration control in a nonlinear metastructure: A spectro-spatial analysis. *J. Sound. Vib.* **2020**, *473*, 115215. [CrossRef]
24. Kalderon, M.; Mantakas, A.; Antoniadis, I. Dynamic Modelling and Experimental Testing of a Dynamic Directional Amplification Mechanism for Vibration Mitigation. *J. Vib. Eng. Technol.* **2023**, 1–12. [CrossRef]
25. Ding, P.; Li, Y.; Shao, L.; Tian, X.M.; Wang, J.Q.; Fan, C.Z. Graphene aperture-based metalens for dynamic focusing of terahertz waves. *Opt. Express* **2018**, *26*, 28038. [CrossRef]
26. Zhu, L.; Dong, L. Electromagnetically Induced Transparency Meta-material: Theories, Designs and Applications. *J. Phys. D Appl. Phys.* **2022**, *55*, 263003. [CrossRef]
27. Niu, X.; Hu, X.; Yan, Q.; Zhu, J.; Cheng, H.; Huang, Y.; Lu, C.; Fu, Y.; Gong, Q. Plasmon-Induced Transparency Effect for Ultracompact On-Chip Devices. *Nanophotonics* **2019**, *8*, 1125–1149. [CrossRef]
28. Wang, T.; Wang, L.M.; Ma, Z.D.; Hulbert, G.M. Elastic analysis of auxetic cellular structure consisting of re-entrant hexagonal cells using a strain-based expansion homogenization method. *Mater. Des.* **2018**, *160*, 284–293. [CrossRef]
29. Davood Mousanezhad; Babak Haghpanah; Ranajay Ghosh; Abdel Magid Hamouda; Hamid Nayeb-Hashemi; Ashkan Vaziri, Elastic properties of chiral, anti-chiral, and hierarchical honeycombs: A simple energy-based approach. *Theor. Appl. Mech. Lett.* **2016**, *6*, 81–96. [CrossRef]
30. Wu, W.; Tao, Y.; Xia, Y.; Chen, J.; Lei, H.; Sun, L.; Fang, D. Mechanical properties of hierarchical anti-tetrachiral metastructures. *Extrem. Mech. Lett.* **2017**, *16*, 18–32. [CrossRef]
31. He, J.; Wang, M.; Zhou, Y.; Pan, Y.; Sun, B. *Optimal Design of Satellite Antenna Based on Sandwich Structure with a Novel Re-Entrant Honeycomb Considering Thermal Load*; IOP Publishing Ltd.: Bristol, UK, 2022.
32. Novak, N.; Krstulovi´c-Opara, L.; Ren, Z.; Vesenjak, M. Mechanical properties of hybrid meta-material with auxetic chiral cellular structure and silicon filler. *Compos. Struct.* **2020**, *234*, 111718. [CrossRef]
33. Quan, C.; Han, B.; Hou, Z.; Zhang, Q.; Tian, X.; Lu, T.J. 3d printed continuous fiber reinforced composite auxetic honeycomb structures. *Compos. B Eng.* **2020**, *187*, 107858. [CrossRef]
34. Chronopoulos, D.; Antoniadis, I.; Ampatzidis, T. Enhanced acoustic insulation properties of composite metamaterials having embedded negative stiffness inclusions. *Extrem. Mech. Lett.* **2017**, *12*, 48–54. [CrossRef]
35. Razgordanisharahi, A.; Ghassabi, A.A.; Hellmich, C. Free vibration analysis of cylin-drical honeycomb sandwich panels using state-space Levy method. *Thin-Walled Struct.* **2023**, *182*, 110308. [CrossRef]
36. Jiang, W.M.; Zhou, J.M.; Liu, J.Y.; Zhang, M.G.; Huang, W. Free vibration behaviours of composite sandwich plates with reentrant honeycomb cores. *Appl. Math. Model.* **2023**, *116*, 547–568. [CrossRef]

37. Li, C.; Shen, H.S.; Wang, H.; Yu, Z. Large amplitude vibration of sandwich plates with functionally graded auxetic 3D lattice core. *Int. J. Mech. Sci.* **2020**, *174*, 105472. [CrossRef]
38. Sabat, R.; Cochin, E.; Kalderon, M.; Lévêque, G.; Antoniadis, I.; Djafari-Rouhani, B.; Pennec, Y. Low frequency sound isolation by a metasurface of Helmholtz ping-pong ball resonators. *J. Appl. Phys.* **2023**, *134*, 144502. [CrossRef]
39. Paradeisiotis, A.; Kalderon, M.; Antoniadis, I. Advanced negative stiffness absorber for low-frequency noise insulation of panels. *AIP Adv.* **2021**, *11*, 065003. [CrossRef]
40. Mukherjee, S.; Scarpa, F.; Gopalakrishnan, S. Phononic band gap design in honey-comb lattice with combinations of auxetic and conventional core. *Smart Mater. Struct.* **2016**, *25*, 054011. [CrossRef]
41. Gao, X.; Wei, J.; Huo, J.; Wan, Z.; Li, Y. The vibration isolation design of a re-entrant negative poisson's ratio meta-material. *Appl. Sci.* **2023**, *13*, 9442. [CrossRef]
42. Liu, J.K.; Liu, H.T.; Li, J. Thermal expansion and bandgap properties of bi-material triangle re-entrant honeycomb with adjustable Poisson's ratio. *Int. J. Mech. Sci.* **2023**, *242*, 108015. [CrossRef]
43. Ding, W.; Chen, T.; Yu, D.; Chen, C.; Zhang, R.; Zhu, J.; Assouar, B. Isotacticity in chiral phononic crystals for low-frequency bandgap. *Int. J. Mech. Sci.* **2023**, *621*, 108678. [CrossRef]
44. Fei, X.; Jin, L.; Zhang, X.; Li, X.; Lu, M. Three-dimensional anti-chiral auxetic meta-material with tunable phononic bandgap. *Appl. Phys. Lett.* **2020**, *116*, 021902. [CrossRef]
45. Bergamini, A.; Miniaci, M.; Delpero, T.; Tallarico, D.; Van Damme, B.; Hannema, G.; Leibacher, I.; Zemp, A. Tacticity in chiralphononic crystals. *Nat. Commun.* **2019**, *10*, 4525. [CrossRef]
46. Ma, N.; Han, Q.; Han, S.; Li, C. Hierarchical re-entrant honeycomb metamaterial for energy absorption and vibration insulation. *Int. J. Mech. Sci.* **2023**, *250*, 108307. [CrossRef]